www.czasopisma.pan.pl PAN POLSKA AKADEMIA NAUK www.journals.pan.pl

PAN ARCHIVES OF ACOUSTICS
Vol. **44**, No. 1, pp. 105–116 (2019)
DOI: 10.24425/aoa.2019.126357

Hybrid Artificial Boundary Conditions for the Application of Blunt-Body Aerodynamic Noise Prediction

Ruixian MA[(1)]*, Zhansheng LIU[(1)], Con J. DOOLAN[(2)]
Danielle J. MOREAU[(2)], Michał CZARNECKI[(3)]

[(1)] *School of Energy Science and Engineering*
Harbin Institute of Technology
Harbin, 150001, Heilongjiang, China
*Corresponding Author e-mail: earlybirdmrx@gmail.com

[(2)] *School of Mechanical and Manufacturing Engineering*
University of New South Wales
Sydney, 2052, NSW, Australia

[(3)] *Faculty of Mechanical Engineering and Aeronautics*
Rzeszów University of Technology
Al. Powstańcow Warszawy 8, 35-959, Rzeszów, Poland

(*received April 16, 2018; accepted September 24, 2018*)

A hybrid artificial boundary condition (HABC) that combines the volume-based acoustic damping layer (ADL) and the local face-based characteristic boundary condition (CBC) is presented to enhance the absorption of acoustic waves near the computational boundaries. This method is applied to the prediction of aerodynamic noise from a circular cylinder immersed in uniform compressible viscous flow. Different ADLs are designed to assess their effectiveness whereby the effect of the mesh-stretch direction on wave absorption in the ADL is analysed. Large eddy simulation (LES) and FW-H acoustic analogy method are implemented to predict the far-field noise, and the sensitivities of each approach to the HABC are compared. In the LES computed propagation field of the fluctuation pressure and the frequency-domain results, the spurious reflections at edges are found to be significantly eliminated by the HABC through the effective dissipation of incident waves along the wave-front direction in the ADL. Thereby, the LES results are found to be in a good agreement with the acoustic pressure predicted using FW-H method, which is observed to be just affected slightly by reflected waves.

Keywords: cylinder aerodynamic noise; non-reflecting boundary conditions; large eddy simulation; FW-H acoustic analogy; acoustic damping layer.

1. Introduction

Exterior aerodynamic noise simulations generally require an external artificial boundary to be non-reflective in order to obtain accurate noise source as well as far-field sound. For direct numerical simulation (DNS) or large eddy simulation (LES), to capture the radiated acoustic waves, high order, low dispersion, and low dissipation numerical schemes are employed, however, spurious waves reflected or generated at the boundaries are also easy to be captured in turn and then propagate back to the domain, contaminating the acoustic field. Meanwhile, non-reflective boundaries are also essential for other acoustic prediction methods, e.g., acoustic analogies (Lighthill, 1952; Lighthill *et al.*, 1954; Curle, 1955; Williams, Hawkings, 1969) in specific problems, because the noise source may be modified by those reflected waves, such as in the prediction of the airfoil tonal noise (Gennaro *et al.*, 2017; Arcondoulis *et al.*, 2013) which is supposed to be generated by the acoustic feedback-loop.

To prevent the wave reflections at the domain edges, non-reflective artificial boundary conditions

(ABC) have been developed through a variety of ways, among which the characteristic boundary conditions (CBC), far-field radiation boundary conditions, and buffer zones are most commonly used. The CBC was proposed by Thompson (1987; 1990) based on the characteristic analysis for hyperbolic system, and Poinsot and Lele (1992) further developed it to Navier-Stokes (N-S) equations, whereby the wave modes (acoustics, vorticity, and entropy) are locally decoupled and identified on the boundaries under the condition of linearity. The amplitudes of outgoing waves are calculated entirely by the upstream variables, whereas the values of incoming pressure waves are linearly relaxed to the imposed value. It is worth noting that this method is typically used for one-dimensional waves perpendicular to the boundaries, which means that oblique incidences or strong mean flow tangential to the boundary affect their performance. New developments on characteristic methods mainly focus on incorporating the treatment of transverse terms to improve the performance at edges and corners for one-dimensional waves (Motheau *et al.*, 2017; Huet, 2015), or broadening this method to two-dimensional waves by linear method for low Mach flow (Yoo, Im, 2007) and by non-linear approach (Liu, Vasilyev, 2010), and also expanding it to three-dimensional flow (Lodato *et al.*, 2008). Recently, the zonal CBC (Sandberg, Sandham, 2006; Gill *et al.*, 2017) were proposed and it shows advantages over traditional methods.

Far-field radiation boundary conditions were originally proposed for hyperbolic systems by Bayliss and Turkel (1982) based on the asymptotic solution to the wave equation, that the solution was matched to a known functional form valid near infinity. The boundary conditions for two-dimensional uniform flow (Tam, Webb, 1993) and non-uniform flow (Tam, Dong, 1994) and for three-dimensional flow (Bogey, Bailly, 2002) were proposed then, respectively. Hixon *et al.* (1995) compared the Thompson, Tam and Webb boundary conditions for the sound radiated by a monopole in uniform mean flow, finding the letter one had the smallest reflected waves. The vital point for the far field boundary is that the sources are expected to be sufficiently far from the boundaries. Once this condition is not satisfied, for example, sources are located near the boundaries, this non-reflective ABC will be degraded.

Most CBCs and far-field methods assume the fluctuation amplitudes in quantities are very small at the boundaries where the non-reflective ABCs are implemented. However, sometimes high amplitude perturbations, such as turbulence, do pass through the boundaries. Moreover, when the viscosity is taken into account, the flow equations are no longer hyperbolic but rather partly parabolic. All of those factors in turn degrade the foregoing non-reflective ABCs. In such cases, a buffer zone is suggested (Fosso *et al.*, 2012; Colonius *et al.*, 1993; Bogey, Bailly, 2002) to treat the nonlinear perturbations, by straightforwardly decreasing the amplitude of turbulent fluctuation as well as that of acoustic waves prior to reaching the boundary. For this purpose, several strategies can be imposed, including adding artificial damping terms or coefficient to the governing equations (Richards *et al.*, 2004; Collis, Lele, 1996; Mimani *et al.*, 2015), and using super-grid-scale technique (Colonius, Ram, 2002; Appelö, Colonius, 2009). For example, to compute the radiated sound accurately for a free shear flow, Colonius *et al.* (1993) suggested an exit zone to attenuate the severe reflections caused by vertical structures at the outflow. The computational domain was extended along the downstream direction to construct the exit zone, where the grid is stretched together with the implementation of a low-pass filter. The coarse grid makes the disturbances poorly resolved thus reducing the nonlinear effect, subsequently, the unresolved disturbances are attenuated by the filter. In such a way, the reflections from the vertical flow were found to be decreased by 3 orders of magnitude.

Many of the above non-reflective ABCs have been evaluated in practical problems, including the jet noise (Christopher, 1998; Hayder, Turkel, 1995; Lodato *et al.*, 2008) and the duct acoustic problem (Richards *et al.*, 2004), in laminar flow past a circular cylinder (Pirozzoli *et al.*, 2013), as well as in turbine blades (Granet *et al.*, 2010; Koupper *et al.*, 2014). In general, it is suggested that the buffer zone performs better than the CBC or far field methods in these specific flows. Even so, preventing spurious acoustic waves from the outflow keeps a challenging task for ABCs in real applications due to the complexity of practical problems such that the significant nonlinear effects may be involved at the outlet when the domain, specifically the irregular computational domain, is truncated. This also leads to another fact that the effectiveness of non-reflective ABCs depends on the problems studied, because the non-reflective ABCs involves a number of free parameters which can only be optimised by experience and trail according to many factors, e.g., flow structures, incident angle and frequency of the waves, and profile of damping function, etc. For instance, in the application of a buffer zone the artificial damping must be treated carefully to avoid waves to be reflected by the absorbing layer itself. Therefore, experience and case dependency of those free parameters is a great obstacle when one expects to quickly predict the far-field noise with the minimum computational cost.

In light of the background provided, it is noticed that no work is reported yet which analyses the effectiveness of the mesh-stretch based acoustic-wave-absorption technique in relation to the pattern of noise propagation. Naturally, how to construct such a zone to be as effective as possible is not fully un-

derstood for the blunt-body aerodynamic noise prediction when complex acoustic propagation pattern is involved, wherein the acoustic radiation field interferes with hydrodynamic field, and meanwhile, the convective effect on wave propagation is non-negligible. Additionally, the impact of mesh-stretch zone on the performance of FW-H, which is another widely used method in far-field noise prediction, also lacks evaluation. In view of the foregoing issues, the main objective of the current paper is to develop an improved non-reflective HABC method which combines a volume-mesh-stretch-based acoustic damping layer (ADL) and the local CBC, through the ADL optimisation by stretching the mesh in the directions considering the wave propagation character. The benchmark problem of a circular cylinder in a subsonic flow is considered to demonstrate the method. Opposite to extending the computational domain, we use a biased mesh stretching strategy in an interior ADL and focus our attention on three points. Firstly, the effectiveness of the HABC on preventing acoustic wave reflections at the very truncated edges. Subsequently, verification of how the acoustic results predicted by LES computation and FW-H acoustic analogy method are affected by the HABC. Thirdly, understanding the relationship between the mesh-stretching direction in the ADL and corresponding ability of damping acoustic waves with a view to improve the efficiency of wave absorption.

2. Computational approach

2.1. Noise-source/flow simulation method

2.1.1. Governing equations

The aerodynamic noise sources, including dipole force and quadruple stress sources, are calculated by solving the compressible N-S equations using LES method. Free-stream velocity U_0^*, temperature T_0^*, density ρ_0^*, unit reference length L^*, flow time t^*, and sound speed c_0 are adopted to obtain the dimensionless flow velocity u_i, temperature T, density ρ, and pressure p, Cartesian coordinates x_i, time t, and Mach number M, as Eqs (1) show

$$u_i = \frac{u_i^*}{U_0^*}, \qquad T = \frac{T^*}{T_0^*}, \qquad \rho = \frac{\rho^*}{\rho_0^*},$$
$$p = \frac{p^*}{\rho_0^* \left(U_0^*\right)^2}, \qquad x_i = \frac{x_i^*}{L^*}, \qquad t = \frac{t^* U_0^*}{L^*}, \tag{1}$$
$$M = \frac{U_0^*}{c_0},$$

where the asterisks denote the dimensional parameters. It is worth noting that the flow variables are composed of a mean flow component and a perturbation component. For instant, the flow velocity $u_i$can be decomposed into $u_i = \overline{u}_i + u_i'$, where the latter fluctuation component u_i' denotes the acoustic particle velocity in the far-field.

The fluid is assumed to be an ideal gas with a constant specific heat ratio $\gamma = 1.4$. The viscosity μ is temperature dependent and the Surtherland law is employed

$$\mu = T^{3/2} \frac{1 + R_{su}}{T + R_{su}}, \tag{2}$$

where R_{su} is the ratio of the Surtherland constant S to T_0, which equals to 0.36867.

Based on the above definitions, the dimensionless continuity, N-S and energy equations can be expressed by

$$\frac{\partial \rho}{\partial t} + \frac{\partial}{\partial x_i}\left(\rho u_i\right) = 0, \tag{3}$$

$$\frac{\partial}{\partial t}\left(\rho u_i\right) + \frac{\partial}{\partial x_i}\left(\rho u_i u_j\right) = -\frac{\partial p}{\partial x_i}\delta_{ij} + \frac{\partial}{\partial x_i}\tau_{ij}, \tag{4}$$

$$\frac{\partial}{\partial t}\left(\rho E\right) + \frac{\partial}{\partial x_i}\left(\rho u_i E\right) = \frac{\partial p}{\partial x_i}\left[u_j \tau_{ij} - u_i p - q_i\right], \tag{5}$$

where δ_{ij} signifies the Dirac-Delta function,

stress tensor $\tau_{ij} = \dfrac{\mu}{\mathrm{Re}}\left(\dfrac{\partial u_i}{\partial x_j} + \dfrac{\partial u_j}{\partial x_i} - \dfrac{2}{3}\dfrac{\partial u_j}{\partial x_j}\delta_{ij}\right)$,

total energy $E = \dfrac{T}{\gamma\left(\gamma - 1\right) M^2} + \dfrac{1}{2u_i^2}$,

and heat flux $q_i = \dfrac{-\mu}{\left(\gamma - 1\right) M^2 \mathrm{Pr}\,\mathrm{Re}}\dfrac{\partial T}{\partial x_i}$

in which the Prandtl constant satisfies $\mathrm{Pr} = 0.72$. The N-S equations are enclosed by the dimensionless ideal gas law $p = (\rho T)/(\gamma M^2)$.

2.1.2. Hybrid artificial boundary condition

A two-dimensional circular cylinder is used to demonstrate the HABC. The cylinder is immersed in a uniform flow at Mach number $M = 0.4$, and Reynolds number $\mathrm{Re} = 3{,}000$ with the cylinder diameter D_{cyl} as character length, in which case the flow is transforming from laminar to turbulence. Figure 1 illustrates the

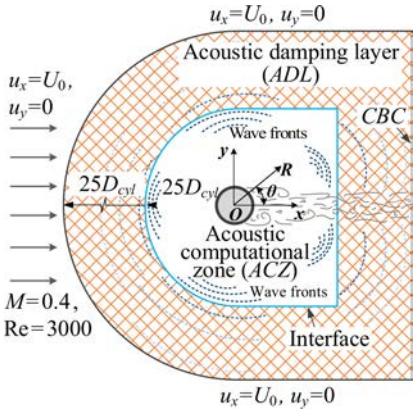

Fig. 1. Computational model and sketch of HABC.

computational model and the sketch of the HABC. The distance from the computational boundaries to the origin O, i.e., cylinder centre, is $50D_{\mathrm{cyl}}$. Uniform velocities ($u_x = U_0$, $u_y = 0$) are defined on the inlet, upper, and lower boundaries, and the right edge of the simulation zone is set as pressure outlet. The cylinder walls are set as no-slip boundaries. Furthermore, for the convenience of analysing the results, R is defined as the distance to the origin calculated by $R = (x^2+y^2)^{1/2}$ and θ denotes the angle between the vector $\mathbf{R}$ and positive x axis.

In order to prevent acoustic wave reflections at the outlet, the local CBC (Poinsot *et al.*, 1992) and far field (Bayliss, Turkel, 1982) boundary conditions are introduced to the outlet, successively and they are presented by "Poinsot BC" and "Far-field BC", respectively, in this paper. Nevertheless, it is noticed during the simulations that above local face-based non-reflective methods are not sufficiently effective to eliminate unphysical (spurious) reflections, resulting in the acoustic field being contaminated gravely. Given this, the whole fluid domain is split into two parts by an interface: an acoustic computational zone (ACZ) and an ADL, as depicted in Fig. 1. Among the two zones, the LES simulation is performed in the former zone and the latter one plays a role of acoustic absorbing layer, wherein waves are damped in a "forward-back" manner. First damping of the forward radiated acoustic waves (incident waves) from the noise sources gradually takes place, e.g., waves scattered by the cylinder walls and those radiated directly by the unsteady wake. Then only a few weak waves might reach the boundaries where the Poinsot BC is applied. Next, further damping of the back reflected acoustic waves by the outflow follows. Simultaneously, the vortices in the wake are dissipated as well before they interact with the outlet boundary, which definitely will improve the performance of the Poinsot BC. Here, the thickness of the ADL is set equal to $25D_{\mathrm{cyl}}$, same as the ACZ. The stretched structural mesh in the ADL is biased to guarantee a smooth growth from the interface with the ACZ, but they keep independent from each other logically. In such a way, a more systematic investigation on the mesh stretching methodology is allowed, in other words, various ADLs can be designed. In the present research, three mesh stretching methods in the ADL are studied. They are a one-dimensional stretch in the direction of wave front (named by 1D-WF-stretch) and of wave tangential (1D-WT-stretch), respectively, and a two-dimensional stretch in both directions represented by 2D-stretch. Afterwards, the HABC is put forward on the basis of 2D-stretch. For a cylinder in a uniform flow, corresponding acoustic radiation pattern had been theoretically proven to be a dipole type (Curle, 1955) at low Mach numbers, therefore, the directions of the wave front and wave tangential, respectively, correspond the radial and tangential directions of the cylinder, ideally, if the effect of convection is negligible.

Figures 2a and 2b demonstrate the comparison of mesh size between various ADLs and baseline on the horizontal centre line ($y = 0$) and at the outlet ($x = 50D_{\mathrm{cyl}}$), respectively, wherein the dimensions are normalised by the cylinder diameter. The baseline is the case without the ADL, also corresponding to case 3 in Table 1, which is shown later. For all simulations, the spatial mesh resolutions in the ACZs are practically coincident, as Fig. 2a shows. O-type grid is adopted in all zones to obtain a high quality structural mesh. As the ACZ is used to directly capture acoustic waves, high resolution grid is implemented in this zone: the thicknesses of the innermost cell and the outermost cell to the cylinder surface are $\Delta x_{\min} = D_{\mathrm{cyl}}/200$, and $\Delta x_{\max} = D_{\mathrm{cyl}}/3$, respectively. On the contrary, in the ADL, large grid spacing is adopted, so that the cell thickness of last layer is $\Delta x_{\max} = 6.3D_{\mathrm{cyl}}$.

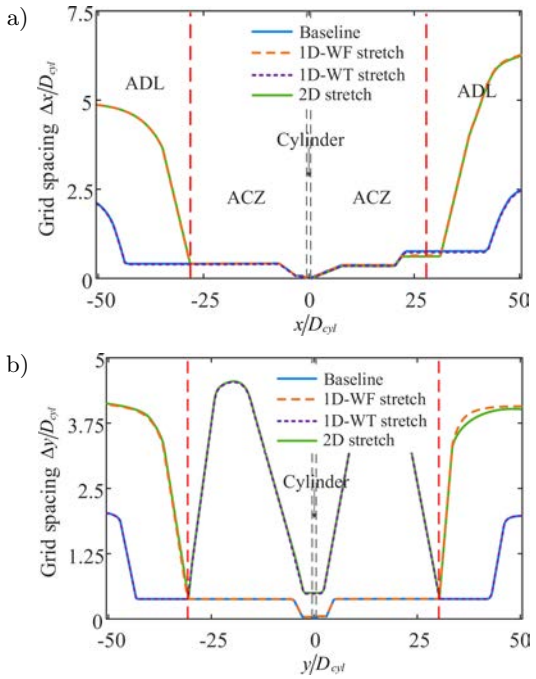

Fig. 2. Mesh size distributions: a) on the horizontal line through the cylinder centre, $y = 0$, b) at the outlet.

2.1.3. Numerical method

Equations (3)–(5) are filtered and then numerically solved by a finite volume scheme using LES method with the dynamic Smagorinsky Sub-Grid Scale (SGS) turbulence model, which has the advantage of viscosity dissipation correction over the ordinary SGS model (Germano *et al.*, 1991). A density based implicit solver is employed in conjunction with a second-order accurate central-difference method for transient formulation. The standard upwind Roe's flux-difference splitting algorithm (Roe, 1986) is chosen to calculate the flux term and the third-order MUSCL

Table 1. Computational results and comparison with previous data.

	$N_\theta \times N_r$	St	$\overline{C}_d$	θ_{sep}	$\overline{u}_{x\,\min}/U_0$
Case 1	125×151	0.198	1.68	82°	−0.192
Case 2	205×180	0.205	1.34	82°	−0.280
Case 3	266×245	0.210	1.26	84°	−0.268
DNS (Dong *et al.*, 2006)	–	0.203	–	–	−0.291
LES (Kravchenko, Moin, 2000)	–	0.21	1.04	88°	−0.37
Experiment (Ong, Wallace, 1996)	–	0.215 ± 0.005	0.99 ± 0.05	$86° \pm 2$	-0.24 ± 0.1
Experiment (Parnaudeau *et al.*, 2008)	–	0.208 ± 0.002	–	–	−0.34

method (Leer, 1979) is employed for spatial discretisation. The time step size is $\Delta t = 2 \cdot 10^{-4}$ s, resulting in a Courant-Friedrichs-Lewyz (CFL) number of CFL $= (U_0 \Delta t)/\Delta x_{\min} = 0.67$. The transient solution is initialised with a steady-state flow obtained by a Reynolds averaged Navier-Stokes (RANS) based simulation. A statistically steady state of vortex shedding is established after a non-dimensional time of 25 vortex shedding cycles, then the flow data are collected over a period of 370 cycles.

The mesh and numerical method are verified by comparing the results with previous published data both in simulations and experiments. Three cases with various numbers of meshes are presented in this study. Shown in Table 1 are values of Strouhal number (also is the dimensionless tonal noise frequency, defined as St $= (f_{\text{vortex}} \cdot D_{\text{cyl}})/U_0$ where f_{vortex} is the vortex shedding frequency gained from fluctuating lift data), mean drag coefficient ($\overline{C}_d$), separation angle (θ_{sep}), and dimensionless mean velocity in the inflow direction ($\overline{u}_{x\,\min}/U_0$). It is found that the finest mesh (case 3) is in the relatively best agreement with the experimental data (Ong, Wallace, 1996; Parnaudeau *et al.*, 2008) and two previous simulations, i.e., the 3-D DNS (Dong *et al.*, 2006) and 3-D LES (Kravchenko, Moin, 2000). However, the mean drag coefficient $\overline{C}_d$ is noticed to be overestimated. This disagreement should be attributed to the 2-D simulation performed in the present paper. Even the Reynolds number is low, the cylinder flow field is three-dimensional in reality (Kravchenko, Moin, 2000). In spite of $\overline{C}_d$, other flow parameters are fairly well agreed with the references. Considering the fact that this study focuses on an enhanced acoustic wave absorbing method and its impacts on acoustic prediction, the numerical method for aerodynamic calculation is thought to be reasonable.

2.2. Acoustic prediction method

As stated earlier, LES is used to simulate the flow field, meanwhile, directly computing acoustic waves. Also as it is known, the acoustic pressure can be interpreted as the fluctuation component of pressure p, which denotes the fluid static pressure in Eqs (4) and (5), in the far field. Thereby, a decomposition is applied to p at each computational node, given as

$$p = \overline{p} + p', \tag{6}$$

where $\overline{p}$ and p' denote the mean pressure and the relevant fluctuation value, respectively. Then, p' will be used to demonstrate the acoustic pressure computed by LES in the following parts of this article.

Formulation 1A of FW-H equation (Brentner, 1987) is employed as well to predict the far-field noise at observation locations using noise sources extracted from LES flow simulation. Actually, the dipole sources from the viscosity-force fluctuation are negligible compared with the pressure fluctuation (Howe, 1998), and further the volume quadrupole sources are also neglected as they are proven much less important when the Mach number is low (Curle, 1955). As a result, the pressure fluctuation is an exclusive noise source now. Taking the rigid cylinder walls as the impermeable integral surface, far-field sound pressure $p'(\mathbf{x}, t)$ at location $\mathbf{X}$ and receiver time t can be computed by

$$4\pi p'(\mathbf{x}, t) = \frac{1}{c_0} \int_{r=0} \left[\frac{\dot{L}_r}{r\,(1 - M_r)^2} \right] \mathrm{d}S, \tag{7}$$

where $r = 0$ represents the cylinder surface, and r is the distance between each source node and the observer. Furthermore, $\dot{L}_r$ is the noise source, here $\dot{L}_r = \partial p/\partial \tau$, and τ represents the source time, which has a relationship with receiver time t of $\tau = t - r/c_0$. Additionally, the Mach number with respect to the observer in the direction of noise radiation is denoted by M_r, and it can be calculated by $M_r = M_i n_i$, where M_i means the Mach number component in Cartesian coordinate system, and n_i is the i component of the outward unit vector normal to the wall.

3. Results and analysis

3.1. Acoustic propagation field

Figures 3a–3c show the instantaneous propagation fields of fluctuation pressure obtained by LES for baseline, Poinsot BC, and Far-field BC, respectively.

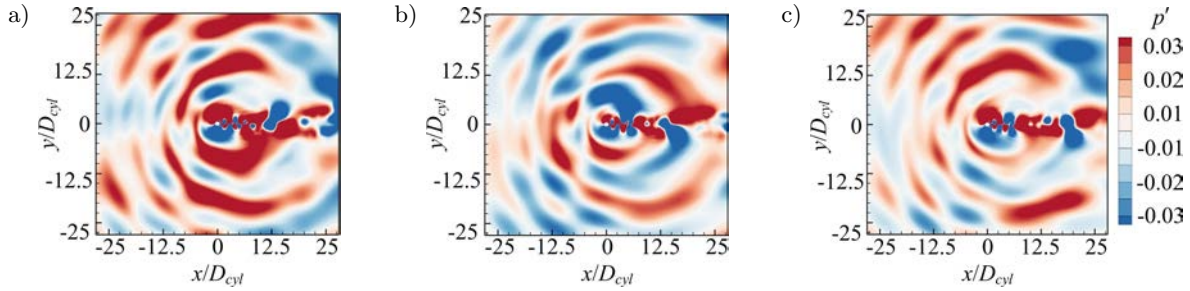

Fig. 3. Instantaneous contours of fluctuation pressure at the 262th vortex shedding cycle: a) baseline, b) Poinsot BC, c) Far-field BC.

As it can be observed, all of the fields are fulfilled with widespread concentrated pressure spots instead of a clean dipole radiation pattern. It is not surprising to obtain contaminated pressure fields for the baseline case (Fig. 3a) as no acoustic treatment, i.e., non-reflective ABC, is applied to the outlet boundary, resulting in the radiated acoustic waves interfering with reflected waves. However, as far as the pressure contours can tell, little evidence of attenuation of the wave interference can be viewed in Figs 3b and 3c when the Poinsot BC and Far-field BC are introduced separately.

Figures 4a and 4b show the instantaneous contours of the dimensionless velocity magnitude and spanwise vorticity. Each flow field shows the unsteady wake is not fully dissipated, such as the tangential velocity gradient and the vortex, when they reach the computational edge where the local non-reflective boundary is applied. Thus the non-reflective ABCs' capability of acoustic absorption is degraded, resulting in the acoustic waves being reflected back into the computational domain.

Depicted in Figs 5a–5d are the fluctuation pressure fields simulated directly through LES at the 262th vortex shedding cycle when 1D-WT-stretch, 1D-WF-stretch, 2D-stretch, and HABC are employed, respectively. As shown in Fig. 5a, the widely distributed pressure spots indicate waves are still being reflected. In Fig. 5b a much more regular dipole character of fluctuation pressure is obtained, with most interference spots being eliminated. Clearer acoustic radiation fields are shown in Fig. 5c and Fig. 5d using the 2D-stretch and HABC methods, respectively. In Fig. 5d, the pseudo sound (hydrodynamic pressure fluctuating in a high amplitude) in the cylinder wake which interferes with acoustic waves in the downstream of the cylinder can be observed. The fluctuation pressure shows a dipole pattern overall, but a weaker quadrupole sources can be also observed in the downstream of the cylinder. The convective effect on wave propagation is indicated by the inclined propagation angles along the upstream direction. The symbols $\oplus$ and $\ominus$ in Fig 5d denote the peak-value positions of the positive and negative pressure pulses respectively It can be seen that the fluctuation pressure pulses propagate along the directions of $\theta = 111°$ (i.e., $\theta = 180° - 69°$) and $\theta = 249°$

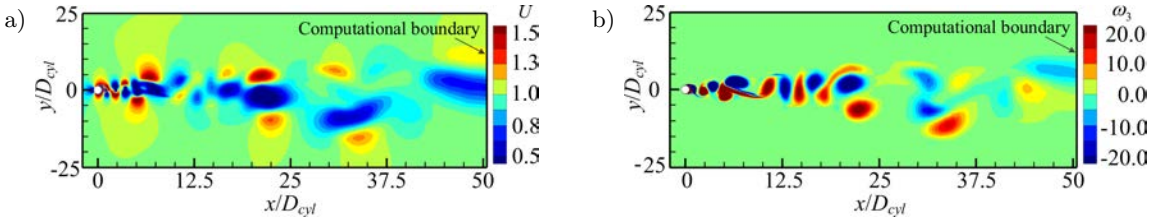

Fig. 4. Instantaneous contours of flow parameters: a) velocity magnitude U, b) spanwise vorticity ω_3.

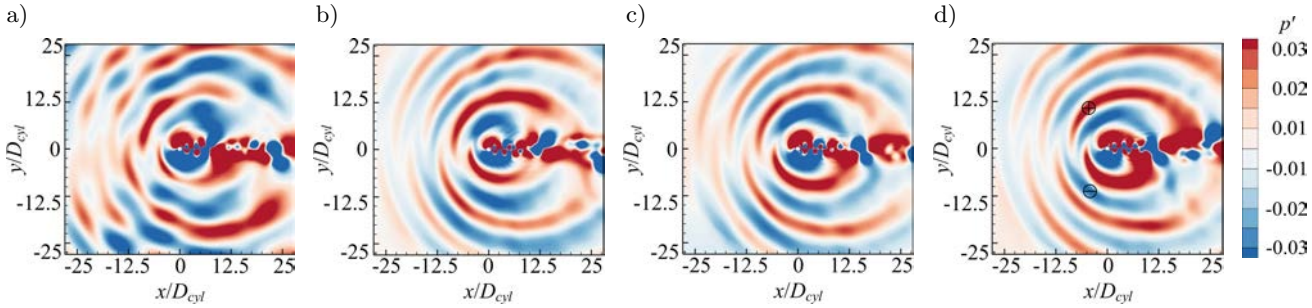

Fig. 5. Instantaneous contours of fluctuation pressure at the 262th vortex shedding cycle: a) 1D-WT-stretch, b) 1D-WF-stretch, c) 2D-stretch, d) HABC.

(i.e., $\theta = 180° + 69°$), rotated about 21° from the vertical orientation to the upstream direction by the convection flow, also exhibiting a deviation of $\approx 2.6°$ with the analytical result of $\theta = 180° \pm 66.4°$ computed by $\theta = \cos^{-1} M$ (Inoue, Hatakeyama, 2002). It should be noted that the analytical solution is approximated for low Mach flow ($M \ll 1$), thus, the small deviation should be acceptable as a relatively high Mach number is considered in the current study. Overall, it is suggested by Figs 4 and 5 that the enhancement of the ADL for acoustic absorption depends on the mesh stretch method, that stretching the mesh in the wavefront direction plays a major role in damping acoustic waves. On the contrary, stretching the mesh in the direction of wave tangential in the ADL absorbs very finite acoustic waves.

3.2. Acoustic spectrum and directivity

Figures 6a and 6b present the comparison of the power spectral density (PSD) of sound pressure calculated by LES and FW-H methods for baseline, Poinsot BC and HABC at two observation positions, i.e. $(0,\ 20D_{\mathrm{cyl}})$ right above the cylinder centre, and $(-20D_{\mathrm{cyl}},\ 0)$ at the cylinder upstream direction, respectively. LES and FW-H methods are plotted by solid and dashed lines, respectively. Two kinds of noise can be observed in Fig. 6: tonal noise at multiple frequencies and broadband noise in the low frequency range.

In Fig. 6a, it can be seen that the tonal noise appears at vortex shedding frequency f_{vortex} ($\mathrm{St} = 0.21$), which is also the cut-off frequency of the free shear layer by the vortex on the opposite side in the cylinder wake, as well as the sidebands and harmonics, showing a good similarity among all results. A derivation of 1.2 dB of fluctuation amplitude at vortex shedding frequency is observed between the baseline and HABC results for LES, whilst a difference of only 0.3 dB is observed for FW-H method. Additionally, the PSD at most tonal noise frequencies are around 1.8 dB smaller in LES in comparison with FW-H. The derivation between the two methods is attributed to the dissipation induced by numerical algorithm in LES. Efforts have been made to eliminate the disagreement by using a finer mesh with a view to decrease the spatial dissipation in the ACZ, nevertheless, it turns out that only negligible improvement can be obtained. By contrast, the second-order accuracy in time and third-order accuracy in space utilised by LES tends to introduce significant numerical dissipation to the acoustic waves during their propagation.

The broadband noise is distributed over low frequency region (typically, $\mathrm{St} < 0.21$), however, it is only acquired in LES results. In fact, the broadband noise might be influenced by two factors: the interference between radiated acoustic waves and reflected waves, and the turbulent flow behind the cylinder. The impact of the interference is indicated by the reduction of low frequency noise after the HABC is implemented, since the maximum reduction of 16 dB is observed in conjunction with the elimination of wave interferences in Fig. 5d, as compared to the baseline results. The broadband noise is also produced by the turbulence in the cylinder wake, which is known as the volume-distributed quadrupoles. Since the sound pressure in LES is directly computed through the flow simulation, the contributions from all noise sources are involved in the according pressure fluctuation, as it can be seen in Fig. 5d. Furthermore, it is noteworthy that to save computational cost the size of the ACZ is truncated to be $25D_{\mathrm{cyl}}$, and the distance from the acoustic observers to the cylinder centre is $r = 20D_{\mathrm{cyl}}$. So the relative distance versus wavelength λ is $r/\lambda = 20 \cdot \mathrm{St} \cdot M = 1.68$, where $\lambda = c_0/f_{\mathrm{vortex}}$. Consequently, the far-field condition $r \gg \lambda$ is not really satisfied at the vortex shedding frequency, let alone lower frequencies, i.e. $\mathrm{St} < 0.21$. Foregoing analysis indicates that it makes sense to obtain broadband low frequency noise at given observers in LES simulation.

For the FW-H results in Fig. 6a, an extreme agreement between the baseline, Poinsot BC and HABC simulations are depicted, indicating that FW-H analogy is much less sensitive to the wave reflections than LES, due to the fact that the fluctuation in the acous-

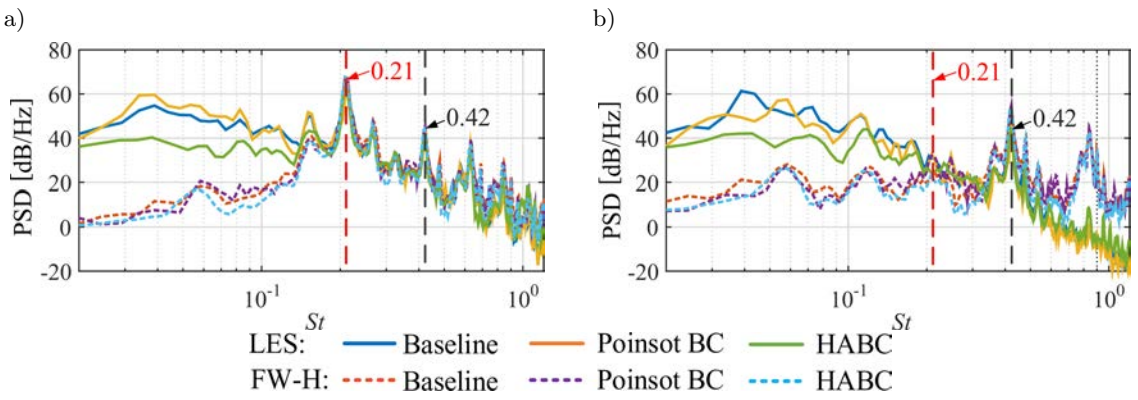

Fig. 6. PSD of acoustic pressure at observers: a) $(0,\ 20\mathrm{D}_{\mathrm{cyl}})$, b) $(-20D_{\mathrm{cyl}},\ 0)$.

tic pressure is much smaller than that in the hydrodynamic pressure. Since the cylinder walls are taken as the noise integral surface for acoustic prediction, the contribution from the reflected waves are overwhelmed by the high-amplitude hydrodynamic component, although those reflected waves can reach the cylinder surface. Subsequently, the effect of interferences on the broadband low frequency noise is not evident. It should also be noted again that the simplified form of FW-H equation, i.e., Eq. (7), implemented in the present study, is derived based on the far-field assumption and the direct sources have been excluded. The deviation in the LES and FW-H results in Fig. 6 over low frequencies may be attributed to these factors.

As shown in Fig. 6b, at the location of the upstream direction, i.e., $(-20D_{\mathrm{cyl}}, 0)$, the tonal noise is noticed at St = 0.42, which represents the secondary harmonic corresponding to the drag. The relationship of a double time between the tonal noise frequencies in Figs 6a and 6b confirms that the lift-force and drag-force generated acoustic waves propagate along the streamwise direction ($y = 0$) and crosswise direction ($x = 0$), respectively (Inoue, Hatakeyama, 2002). Similar reduction of the spectrums at low frequencies is obtained when HABC is employed, as shown in Fig. 6a. The fluctuation amplitudes of acoustic pressure at higher frequencies, such as the tonal noise at quadruple frequency, are underestimated by LES, also suggesting the small acoustic fluctuations are over-dissipated by the temporal/spatial numerical schemes.

Depicted in Fig. 7 is the directivity of overall sound pressure level (OASPL) predicted by LES and FW-H methods, respectively, at $R = 20D_{\mathrm{cyl}}$ for baseline, Poinsot BC, and HABC cases. It again shows that the LES predicted results are much more sensitive to wave reflections than those of FW-H. As it is shown, in LES simulations, the directivity is entirely distorted in the baseline, slightly improved by Poinsot BC (such as in the 180° direction), and well reconstructed to be a dipole pattern by the HABC, respectively, while a small change of 0.23 dB in the directions of 90° and 270° is observed among all FW-H

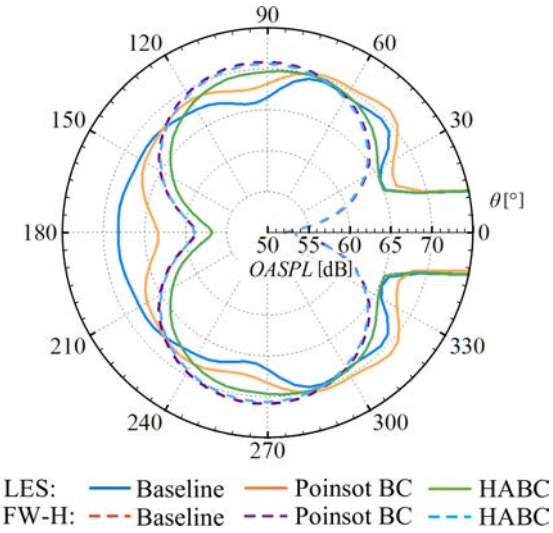

Fig. 7. Directivity of OASPL for different non-reflective ABCs at $R = 20D_{\mathrm{cyl}}$.

predicted OASPL. Using the HABC, the directivity calculated by the two methods is in good agreement at most angular locations, except around the cylinder wake region (approximately from 330° to 30°). This is quite expected due to the presence of large hydrodynamic fluctuations in this region in the flow simulation. On the contrary, only pure acoustic fluctuations whose amplitude is small are acquired through FW-H equation. As the numerical accuracy of LES introduces significant dissipation, a small reduction of OASPL is obtained by LES in comparison with FW-H.

Acoustic results are analysed in more detail for two kinds of ADL, i.e., 1D-WF-stretch and 2D-stretch, with a view to corelate the direction of mesh stretch in the ADL with the performance of wave absorption. The 1D-WT-stretch is not included here considering it is already proved to be less effective. To this end, first, the PSD of sound pressure computed by LES and FW-H methods is depicted in Figs 8a and 8b for the baseline, 1D-WF-stretch, and 2D-stretch at locations $(0, 20D_{\mathrm{cyl}})$ and $(-20D_{\mathrm{cyl}}, 0)$, respectively. It can be seen that the broadband noise at low frequencies is decreased by around 10dB using the ADLs, indi-

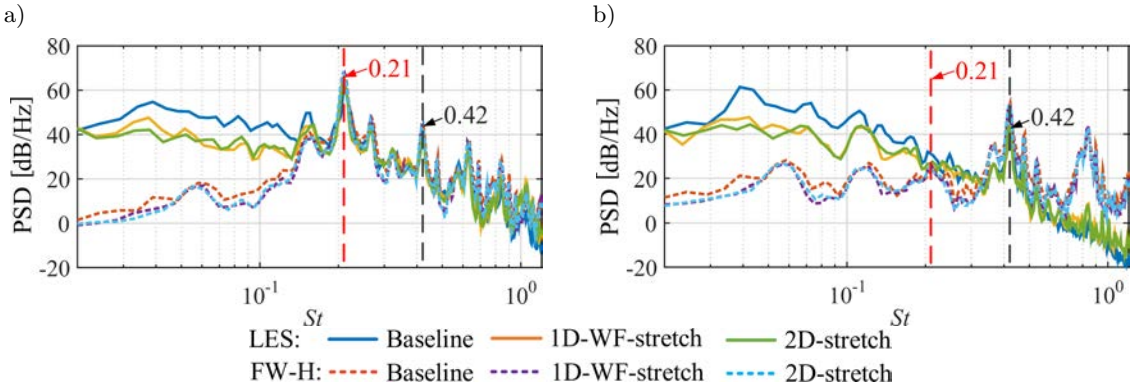

Fig. 8. PSD of acoustic pressure for various ADLs at two locations: a) $(0, 20\mathrm{D}_{\mathrm{cyl}})$, b) $(-20D_{\mathrm{cyl}}, 0)$.

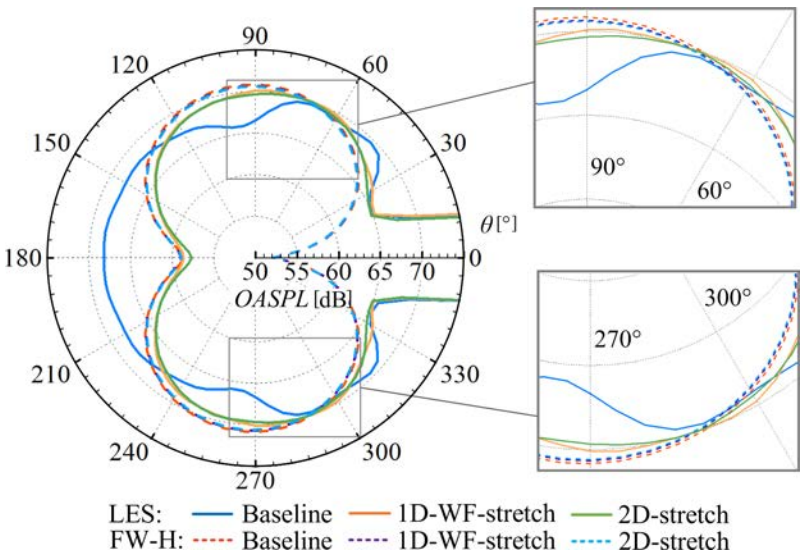

Fig. 9. Directivity of OASPL for various ADLs, $R = 20D_{\mathrm{cyl}}$.

cating the interferences are greatly reduced. Additionally, only a small deviation can be noticed between the PSD of 1D-WF-stretch and 2D-stretch. This similarity suggests a comparative effectiveness of the two methodologies to absorb acoustic waves, in other words, stretching the mesh along the wave-front direction predominates the absorption.

As a supplement for the discussion in Fig. 8, the directivity of OASPL at $R = 20D_{\mathrm{cyl}}$ is compared in Fig. 9 between the baseline, 1D-WF-stretch, and 2D-stretch results computed by LES and FW-H. One can see that a dipole character is well recovered through 1D-WF-stretch in LES simulations. However, in the range of 40°–110° and 250°–320° slight fluctuations of the directivity curve can be noticed, as shown in the enlarged images in the insets. With further expanding of the mesh stretch from one-dimension to two-dimension, i.e., the implementation of 2D-stretch, the fluctuations are eliminated. Substantially, it implies that the reflected acoustic waves are not fully dissipated yet by the 1D-WF-stretch. The remaining weak reflections should be attributed to the convective and turbulent effect, which results in the acoustic waves propagating not in a strict one-dimension (radial direction of the cylinder) manner, but in a multi-dimension way, especially in the downstream region of the cylinder where the acoustic waves interfere with hydrodynamic fluctuations. Therefore, an improvement of acoustic-wave absorption is achieved by the 2D-stretch, as the wave-propagation pattern is better matched to dissipate more waves, and this behaviour can be confirmed by Figs 4b and 4c. Even so, it should be acceptable that stretching mesh along the wave-front direction plays the most important role in damping the reflections for the 2D-stretch ADL.

We now intend to introduce a transformation to the observation locations for directivity analysis proposed by Inoue and Hatakeyama (2002) with a view to have a deeper insight into the convective effect on wave propagation. In order to include the convection in the directivity, the measurement radius with respect to the origin (i.e., the cylinder center) is multiplied by a Doppler factor $\sqrt{1 - M\sin^2\theta'} - M\cos\theta'$, where $\theta' \in [-180°, 180°]$ is the angle between the negative x-axis and the wave propagation direction. The transformation is defined as

$$R' = R\left(\sqrt{1 - M\sin^2\theta'} - M\cos\theta'\right), \tag{8}$$

where R and R' denote the original and corrected distance, respectively. We recall that the earlier directivities in Figs 7 and 9 are taken at $R = 20D_{\mathrm{cyl}}$. Next, Eq. (8) is applied to obtain the directivity of OASPL at the transformed locations for the HABC case, which is chosen to demonstrate the influence of convection on noise propagation.

Shown in Fig. 10 are the directivities of OASPL computed by LES and FW-H approaches using the HABC, wherein the solid and dashed lines denote the results measured at $R = 20D_{\mathrm{cyl}}$ and at $R' = R(\sqrt{1 - M\sin^2\theta'} - M\cos\theta')$ with $R = 20D_{\mathrm{cyl}}$, respectively, and the dashed dark lines marked from the origin denote the direction of the peak OASPL measured at R. It should be noted that the directivities are compared with the results computed by a finite-differential scheme based linearised Euler equations (LEE) (Mimani *et al.*, 2015) solver using the fluctuation force acted on the cylinder, which is extracted from the LES flow simulation, as the dipole noise source term. In such a way, pure acoustic fluctuations are computed in the LEE simulation. A good agreement between the predicted directivities can be observed except in the cylinder wake region where the hydrodynamic pressure dominates the fluctuations. The

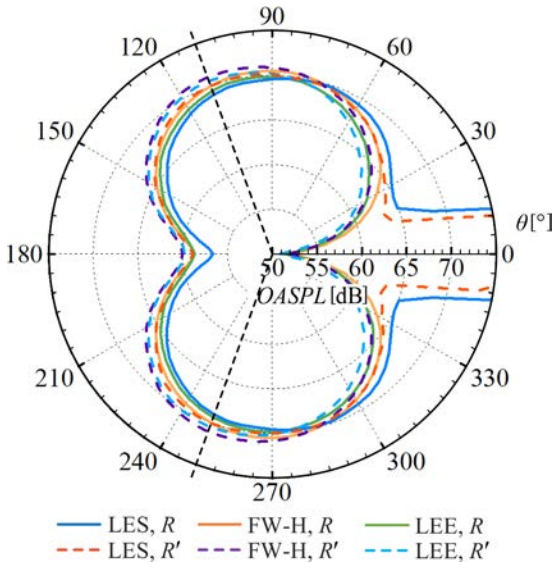

Fig. 10. Directivity of OASPL computed by LES, FW-H using HABC and the comparison with LEE. Solid lines denote the results at $R = 20D_{\mathrm{cyl}}$; dashed lines denote the results at $R' = R(\sqrt{1 - M\sin^2\theta'} - M\cos\theta')$ with $R = 20D_{\mathrm{cyl}}$, $\theta' \in [-180°, 180°]$ (w.r.t. negative x axis).

effect of mean flow on sound propagation is indicated by the dashed directivity curves, so that the acoustic waves propagate to the upstream and downstream directions with amplified and reduced amplitudes, respectively. Additionally, the lobes are inclined along the upstream direction by the convective flow, showing the directivity at $\theta = 180° \pm 69°$, which is consistent with the propagation angle of fluctuation pressure waves in Fig. 5d.

4. Conclusions

This paper has presented an enhanced non-reflective hybrid artificial boundary conditions (HABC) to simulate the aerodynamic noise generated by subsonic flow over a two-dimensional circular cylinder at $M = 0.4$. The HABC makes use of a volume-mesh-stretch based acoustic damping layer (ADL) and the local-face-based characteristic boundary conditions (CBC) (Poinsot, Lele, 1992) to prevent spurious reflections at the exterior boundaries. The effectiveness of the ADL is improved by taking the effect of convection and turbulence on acoustic wave propagation into account using the mesh-stretch technique in a two-dimensional manner. The acoustic propagation fields, power spectral density (PSD) of the sound pressure, and the directivity of overall sound pressure level (OASPL) are recovered to show a dipole pattern using the HABC in the LES simulation, validating the usefulness of the proposed method. On the other hand, a very small deviation between the HABC and baseline results predicted by FW-H is observed, due to the fact that the amplitude of hydrodynamic fluctuations is much higher as compared to the fluctuations induced by reflected waves on the cylinder surface. Using the HABC, the directivity of OASPL predicted by LES and FW-H results are shown to be in a good agreement except in the cylinder wake region where LES reveals high-amplitude hydrodynamic pressure fluctuations because of the vortex shedding. Furthermore, an excellent agreement is also observed between the LES and FW-H computed sound pressure in frequency domain apart from the broadband low frequency noise, which is attributed to the turbulence noise produced by the cylinder wake in the LES simulation. In particular, it is demonstrated that to damp the acoustic waves using the ADL approach, stretching mesh in the direction of the wave front is most effective, nevertheless, a two-dimensional mesh stretch is needed when the wave propagation is affected by convection and the cylinder unsteady wake. Although the benchmark problem of a circular cylinder aerodynamic noise is considered here, it is worth mentioning that the method in the present study can be conveniently extended to more complex flow-induced problems, such as the noise prediction due to acoustic feedback loop in the airfoil (Gennaro *et al.*, 2017; Arcondoulis *et al.*, 2013), where the feedback acoustic waves play an important role in the noise generation on the airfoil surface; this will be a focus of future investigation.

Acknowledgments

The authors would like to thank China Scholarship Council (CSC, Grant No. 201606120129) for the financial support. The simulations were carried out on the High Performance Computing Platforms (Leonardi and Trentino) at the University of New South Wales (UNSW, Sydney). The anonymous reviewers are also sincerely acknowledged.

References

1. Appelö D., Colonius T. (2009), *A high-order super-grid-scale absorbing layer and its application to linear hyperbolic systems*, Journal of Computational Physics, **228**, 11, 4200–4217.

2. Arcondoulis E.J.G., Doolan C.J., Zander A.C., Brooks L.A. (2013), *An experimental investigation of airfoil tonal noise*, Proceedings of Acoustics, Victor Harbor, Australia.

3. Bayliss A., Turkel E. (1982), *Far-field boundary conditions for compressible flows*, Journal of Computational Physics, **48**, 182–199.

4. Bogey C., Bailly C. (2002), *Three-dimensional non-reflective boundary conditions for acoustic simulations:*

far field formulation and validation test cases, ACTA Acustica United with Acustica, **88**, 463–471.

5. Brentner K.S. (1987), *Prediction of helicopter rotor discrete frequency noise: A computer program incorporating realistic blade motions and advanced acoustic formulation*, NASA-TM-87721.

6. Christopher K.W.T. (1998), *Advances in numerical boundary conditions for computational aeroacoustics*, Journal of Computational Acoustics, **6**, 4, 377–402.

7. Collis S., Lele S. (1996), *A computational approach to swept leading-edge receptivity*, Aerospace Sciences Meeting & Exhibit, Reno, NV.

8. Colonius T.I.M., Lele S.K., Moin P. (1993), *Boundary conditions for direct computation of aerodynamic sound generation*, AIAA Journal, **31**, 9, 1574–1582.

9. Colonius T., Ran H. (2002), *A Super-Grid-Scale Model for Simulating Compressible Flow on Unbounded Domains*, Journal of Computational Physics, **182**, 1, 191–212.

10. Curle N. (1955), *The Influence of Solid Boundaries upon Aerodynamic Sound*, Proceedings of the Royal Society A: Mathematical, Physical and Engineering Sciences, **231**, 1187, 505–514.

11. Dong S., Karniadakis G.E., Ekmekci A., Rockwell D. (2006), *A combined direct numerical simulation–particle image velocimetry study of the turbulent near wake*, Journal of Fluid Mechanics, **569**, 185–207.

12. Farassat F. (1981), *Linear acoustic formulas for calculation of rotating blade noise*, AIAA Journal, **19**, 9, 1122–1130.

13. Fosso P.A., Deniau H., Lamarque N., Poinsot T. (2012), *Comparison of outflow boundary conditions for subsonic aeroacoustic simulations*, International Journal for Numerical Methods in Fluids, **68**, 10, 1207–1233.

14. Gennaro M.D., Kuhnelt H., Zanon A. (2017), *Numerical prediction of the tonal airborne noise for a NACA0012 aerofoil at Moderate Reynolds number using a transitional URANS approach*, Archives of Acoustics, **42**, 4, 653–675.

15. Germano M., Piomelli U., Moin P., Cabot W.H. (1991), *A dynamic subgrid-scale eddy viscosity model*, Physics of Fluids, **3**, 7, 1760–1765.

16. Gill J., Fattah R., Zhang X. (2017), *Towards an effective non-reflective boundary condition for computational aeroacoustics*, Journal of Sound and Vibration, **392**, 217–231.

17. Granet V., Vermorel O., Léonard T., Gicquel L., Poinsot T. (2010), *Comparison of Nonreflecting Outlet Boundary Conditions for Compressible Solvers on Unstructured Grids*, AIAA Journal, **48**, 10, 2348–2364.

18. Hayder M.E., Turkel E. (1995), *Nonreflecting boundary conditions for jet flow computations*, AIAA Journal, **33**, 12, 2264–2270.

19. Hixon R., Shih S.-H., Mankabadi R.R. (1995), *Evaluation of boundary conditions for computational aeroacoustics*, AIAA Journal, **33**, 11, 2006–2012.

20. Howe M.S. (1998), *Acoustics of Fluid–Structure Interactions*, Cambridge University Press. Cambridge.

21. Huet M. (2015), *One-dimensional characteristic boundary conditions using nonlinear invariants*, Journal of Computational Physics, **283**, 312–328.

22. Inoue O., Hatakeyama N. (2002), *Sound generation by a two-dimensional circular cylinder in a uniform flow*, Journal of Fluid Mechanics, **471**, 285–314.

23. Koupper C., Poinsot T., Gicquel L., Duchaine F. (2014), *Compatibility of characteristic boundary conditions with radial equilibrium in turbomachinery simulations*, AIAA Journal, **52**, 12, 2829–2839.

24. Kravchenko A.G., Moin P. (2000), *Numerical studies of flow over a circular cylinder at* Re_D = 3900, Physics of Fluids, **12**, 2, 403–417.

25. Leer B.V. (1979), *Towards the ultimate conservative difference scheme.V.A second-order sequel to Godunov's method*, Journal of Computational Physics, **32**, 1, 101–136.

26. Lighthill M.J. (1952), *On Sound Generated Aerodynamically I.General Theory*, Proceeding of the Royal Society of London. Series A, Mathematical and Physical Sciences, **211**, 1107, 564–587.

27. Lighthill M.J., F.R.S. (1954), *On Sound Generated Aerodynamically II. Turbulence as a Source of Sound*, Proceeding of the Royal Society of London. Series A, Mathematical and Physical Sciences, **222**, 1148, 1–32.

28. Liu Q., Vasilyev O.V. (2010), *Nonreflecting boundary conditions based on nonlinear multidimensional characteristics*, International Journal for Numerical Methods in Fluids, **62**, 1, 24–55.

29. Lodato G., Domingo P., Vervisch L. (2008), *Three-dimensional boundary conditions for direct and large-eddy simulation of compressible viscous flows*, Journal of Computational Physics, **227**, 10, 5105–5143.

30. Mimani A., Prime Z., Doolan C.J., Medwell P.R. (2015), *A sponge-layer damping technique for aeroacoustic Time-Reversal*, Journal of Sound and Vibration, **342**, 1244-151.

31. Motheau E., Almgren A., Bell J.B. (2017), *Navier–Stokes Characteristic Boundary Conditions Using Ghost Cells*, AIAA Journal, **55**, 10, 3399–3408.

32. Ong L., Wallace J. (1996), *The velocity field of the turbulent very near wake of a circular cylinder*, Experiments in Fluids, **20**, 441–453.

33. Parnaudeau P., Carlier J., Heitz D., Lamballais E. (2008), *Experimental and numerical studies of the flow over a circular cylinder at Reynolds number 3900*, Physics of Fluids, **20**, 8, 85–101.

34. Pirozzoli S., Colonius T. (2013), *Generalized characteristic relaxation boundary conditions for unsteady compressible flow simulations*, Journal of Computational Physics, **248**, 109–126.

35. Poinsot T.J., Lele S.K. (1992), *Boundary conditions for direct simulations of compressible viscous flows*, Journal of Computational Physics, **101**, 1, 104–129.

36. Richards S.K., Zhang X., Chen X.X., Nelson P.A. (2004), *The evaluation of non-reflecting boundary conditions for duct acoustic computation*, Journal of Sound and Vibration, **270**, 3, 539–557.

37. Reo P.L. (1986), *Characteristic-based schemes for the Euler equations*, Annual Review of Fluid Mechanics, **18**, 1, 337–365.

38. Sandberg R.D., Sandham N.D. (2006), *Nonreflecting zonal characteristic boundary condition for direct numerical simulation of aerodynamic sound*, AIAA Journal, **44**, 2, 402–405.

39. Tam C.K.W., Webb J.C. (1993), *Dispersion-relation-preserving finite difference schemes for computational acoustics*, Journal of Computational Physics, **107**, 262–281.

40. Tam C.K.W., Dong Z. (1994), *Wall boundary conditions for high-order finite-difference schemes in computational aeroacoustics*, Theoretical and Computational Fluid Dynamics, **6**, 5–6, 303–322.

41. Thompson K.W. (1987), *Time dependent boundary conditions for hyperbolic systems*, Journal of Computational Physics, **68**, 1, 1–24.

42. Thompson K.W. (1990), *Time dependent boundary conditions for hyperbolic systems, II*, Journal of Computational Physics, **89**, 2, 439–461.

43. Williams J.E.F., Hawkings D.L. (1969), *Sound generation by turbulence and surfaces in arbitrary motion*, Philosophical Transactions of the Royal Society A: Mathematical, Physical and Engineering Sciences, **264**, 1151, 321–342.

44. Yoo C.S., Im H.G. (2007), *Characteristic boundary conditions for simulations of compressible reacting flows with multi-dimensional, viscous and reaction effects*, Combustion Theory and Modelling, **11**, 2, 259–286.